Chapter 4

Models

Contents

This chapter focuses on the description of models developed to study the stability of clathrate hydrates and the transport of methane in the martian crust. The thermodynamics of the formation or dissociation of clathrates is most often based on the model of van der Waals and Platteeuw (1959), which includes assumptions similar to those used to establish the adsorption theory of Langmuir. Regarding the methane migration, several physical processes can be involved. These processes are reviewed in the following section and are described in more details at the end of this chapter.

4.1   Methane migration in the martian crust and outgassing scenarios

Various possible ways of migration and storage for methane in the martian crust and subsequent discharge into the atmosphere are illustrated in Fig. 4.1. During the whole geological history of Mars, methane formation mechanisms could have taken place in the deep subsurface and could still be active nowadays. After its generation, methane would migrate upwards and be either directly released at the surface or trapped in subsurface reservoirs (clathrates, zeolites or sealed traps) where it could eventually accumulate over long time periods before to be episodically liberated during destabilising events. These phenomena leading to surface degassing imply a change in temperature/pressure conditions of the CH_4 reservoirs and are multiple: faulting and landslide generated by seismicity, impact, climatic changes...
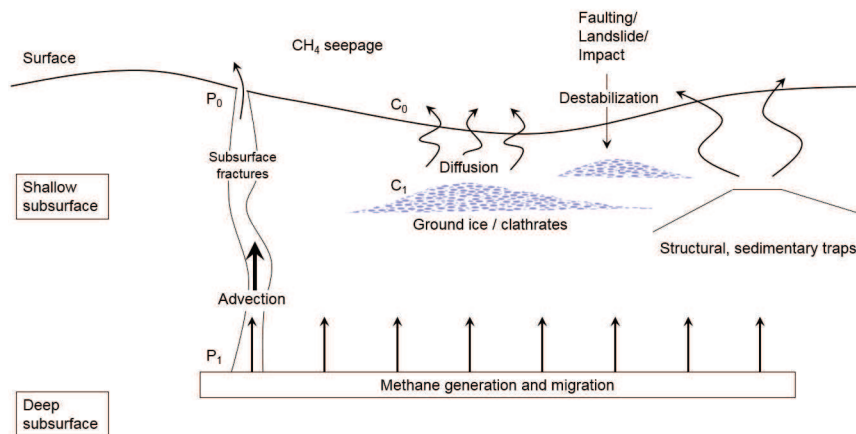

Figure 4.1: Possible scenarios of methane migration and storage in the martian crust and subsequent release into the atmosphere.

When ascending through stratigraphic layers, methane can move via one or several transport mechanisms. Seepage can occur through advection, the main CH_4 transport process on Earth, driven by pressure gradients and permeability and generally associated to fracture networks (Etiope and Oehler, 2019). Therefore, whenever gas pressure increases in subsurface gas pockets or along faults due to decomposition of methane reservoirs for instance or when large variations in pressure above regolith are induced by surface winds, methane may be discharged in the martian atmosphere by advection (Etiope and Oehler, 2019). Another transport mechanism is diffusion, which is mainly controlled by concentration gra-

dients. This process is not efficient on short timescales (Stevens et al., 2017) and short-lived methane plumes related to diffusion should therefore originate from shallow depths.

All the mechanisms of generation, accumulation and migration together control the seepage intensity. In the following, we first describe the storage system modelling.

4.2 Thermodynamic modelling of clathrates

Three main models have been used in the litterature to study clathrate hydrate stability and composition on Mars (Chastain and Chevrier, 2007; Thomas et al., 2009; Herri and Chassefière, 2012) and are all based on the statistical thermodynamic method developed by van der Waals and Platteeuw (1959), which requires the following assumptions (Sloan and Koh, 2007):

1. Each cavity can contain at most one guest molecule.

2. The guest molecules interact only with the nearest neighboring host molecules and guest-guest molecule interactions are neglected. That is, the energy of each trapped gas molecule is independent of the number and nature of other guest molecules.

3. The contribution of water molecules to the free energy is independent of the cavity occupancy. This implies that guest molecules do not distort the cage.

4. The interaction between guest and water molecules can be described by a pair potential function, and the cavity can be treated as perfectly spherical.

5. The ideal gas partition function is applicable to guest molecules. That is the rotational, vibrational, nuclear, and electronic energies are not significantly affected by enclathration. This hypothesis implies that guest molecules can freely rotate in the cavities.

6. The laws of classical statistical mechanics are valid and no quantum effects are needed.

We are interested here in the temperature-pressure conditions of the I-H-V (or L_W-H-V) equilibrium curve presented in Fig. 3.6. Thermodynamic equilibrium implies the minimization of the Gibbs energy and the equality of chemical potentials of water μ_w in the ice phase α (or liquid phase L) and in the clathrate hydrate phase H:

$$\mu_w^H = \mu_w^{L,\alpha} \tag{4.1}$$

For convenience, this equalization can be rewritten in terms of chemical potential differences by introducing a hypothetical phase β that corresponds to a clathrate with empty cavities:

$$\left.\begin{array}{l} \Delta\mu_w^{\beta-H} = \mu_w^{\beta} - \mu_w^H \\ \Delta\mu_w^{\beta-L,\alpha} = \mu_w^{\beta} - \mu_w^{L,\alpha} \end{array}\right\} \rightarrow \Delta\mu_w^{\beta-H} = \Delta\mu_w^{\beta-L,\alpha} \tag{4.2}$$

where μ_w^{β} is the chemical potential of water in the empty clathrate. $\Delta\mu_w^{\beta-H}$ is evaluated via statistical thermodynamics, while $\Delta\mu_w^{\beta-L,\alpha}$ is determined from classical thermodynamics.

Modelling $\Delta\mu_w^{\beta-H}$

Following the model of van der Waals and Platteeuw (1959), this term can be written as a function of the occupancy fraction $\theta_{G,i}$ of a species G in a given type i of cage (i = small or large) for a given type of clathrate structure (I or II) as:

$$\Delta\mu_w^{\beta-H} = -RT \sum_i \nu_i \ln(1 - \sum_G \theta_{G,i}) \tag{4.3}$$

where R is the universal gas constant, T is the thermodynamic temperature and ν_i is the number of cavities of type i per water molecule in the clathrate unit cell. The occupancy fraction is comparable to the fractional coverage of the adsorbed monolayer in the Langmuir gas adsorption theory and is defined as:

$$\theta_{G,i} = \frac{C_{G,i}(T)f_G(T,P)}{1 + \sum_J C_{J,i}(T)f_J(T,P)} \tag{4.4}$$

where $f_G(T,P)$ is the fugacity of the guest G in the gas or liquid phase. The Langmuir constant $C_{G,i}(T)$ is analogous to the equilibrium Langmuir adsorption constant and characterizes the attractiveness of the cavity i for a species G. For a given value of the fugacity, the species with the highest Langmuir constant is the most strongly enclathrated guest in a cavity. Therefore, the gas molecules with an optimal guest/cavity size ratio, as mentioned in Section 3.2, have higher values of $C_{G,i}(T)$. The latter is defined by the following equation:

$$C_{G,i}(T) = \frac{1}{k_B T} \int \int \exp\left(\frac{-W_{G,i}(\boldsymbol{r}, \boldsymbol{\Omega})}{k_B T}\right) d\boldsymbol{r} d\boldsymbol{\Omega} \tag{4.5}$$

where k_B is the Boltzmann constant and $W_{G,i}$ is the interaction potential energy experienced by the guest molecule G included in the cavity i. This interaction is function of the position $\boldsymbol{r}$ and orientation $\boldsymbol{\Omega}$ vectors of the guest molecule in the cage. If the cavity is assumed to be perfectly spherical and the guest molecule can freely rotate in the cage, the Langmuir constant can be written as:

$$C_{G,i}(T) = \frac{4\pi}{k_B T} \int_0^{R_c} \exp\left(\frac{-W_{G,i}(r)}{k_B T}\right) r^2 dr \qquad (4.6)$$

where R_c is the radius of the spherical cavity and $W_{G,i}(r)$ is the spherically averaged potential energy between the guest molecule and the cavity. The interaction potential used in the original work by van der Waals and Platteeuw (1959) is based on the Lennard-Jones 6-12 pair potential. However, McKoy and Sinanoğlu (1963) suggested to derive the interaction potential of Equation 4.6 from the Kihara potential $\Phi_K(r)$, better adapted for both larger and nonspherical molecules. This potential is commonly used in clathrate hydrate stability calculations and is given by:

$$\Phi_K(r) = 4\epsilon\left(\left(\frac{\sigma}{r-2a}\right)^{12} - \left(\frac{\sigma}{r-2a}\right)^6\right) \quad \text{for } r > (a_G + a_w) \quad (4.7a)$$

$$\Phi_K(r) = \infty \quad \text{for } r \leq (a_G + a_w) \qquad (4.7b)$$

where σ is the cores distance at zero potential ($\Phi_K = 0$, attractive and repulsive interactions are equal), a is the radius of the spherical core (the subscript G refers to the guest, while w refers to water) and ϵ is the maximum attractive potential (at $r = \sqrt[6]{2}\sigma$). Averaging the pair potentials of Equation 4.7a and b between the guest and each water molecule at the surface of the spherical cage leads to the expression of the cell potential:

$$W_{G,i}(r) = 2z\epsilon\left[\frac{\sigma^{12}}{R_c^{11}r}\left(\delta^{10} + \frac{a}{R_c}\delta^{11}\right) - \frac{\sigma^6}{R_c^5 r}\left(\delta^4 + \frac{a}{R_c}\delta^5\right)\right] \qquad (4.8)$$

with

$$\delta^N = \frac{1}{N}\left[\left(1 - \frac{r}{R_c} - \frac{a}{R_c}\right)^{-N} - \left(1 + \frac{r}{R_c} - \frac{a}{R_c}\right)^{-N}\right] \qquad (4.9)$$

where z is the coordination number of the cavity. The parameters R_c and z are specific to the type of cage and the clathrate structure. The

Kihara parameters ϵ, a and σ are specific to the guest molecule and are determined by a linear regression fitted to experimental data. The set of Kihara parameters used in the present work is given in Table 4.1. These parameters have been optimized by Herri and Chassefière (2012) in a study where they fitted the model of van der Waals and Platteeuw (1959) to compare the deviation from experimental data of pure clathrate hydrates at temperatures relevant to Mars.

Table 4.1: Kihara parameters used in the present study. These parameters are derived from Herri and Chassefière (2012) for CH_4, CO_2, N_2 and Ar and from Strobel et al. (2009) for H_2.

Molecule	ϵ/k_B (K)	σ (Å)	a (Å)
CH_4	166.36	3.0500	0.3834
CO_2	178.21	2.8730	0.6805
N_2	133.13	3.0993	0.3526
Ar	174.14	2.9434	0.1840
H_2	80.424	3.07838	0.1973

Finally, note that the upper limit for the integral in Equation 4.6 is often written R_c but should be presented as $R_c - a_G$ instead (Sloan and Koh, 2007). Indeed, this latter limit does physically make sense and corresponds to the spherical core of the guest molecule in contact with the edge of the water cavity. Moreover, if care is not taken, problems can appear in the numerical integration to calculate the Langmuir constant because of the division by an r term in Equations 4.8 and 4.9 when $r = 0$ and $r = R_c - a_G$ respectively. Following Pratt et al. (2001) and applying L'Hospital's rule, we obtain:

$$\lim_{r \to 0} W_{G,i}(r) = 2z\epsilon \left[\frac{\sigma^{12}}{R_c^{11}} \left(\delta'^{10} + \frac{a}{R_c} \delta'^{11} \right) - \frac{\sigma^6}{R_c^5} \left(\delta'^4 + \frac{a}{R_c} \delta'^5 \right) \right] \quad (4.10)$$

with

$$\delta'^N = \frac{2}{R_c} \left(1 - \frac{a}{R_c} \right)^{-(N+1)} \quad (4.11)$$

This leads to a finite value of the cell potential. At $r = 0$, using Equations 4.10 and 4.11 will thus give a finite number for the exponential term in Equation 4.6, while the integrand will be zero (because of the r^2 term). Applying the same method for $r = R_c - a_G$, we get:

$$\lim_{r \to R_c - a_G} W_{G,i}(r) = +\infty \quad (4.12)$$

At $r = R_c - a_G$, the exponential term in the Langmuir constant expression will thus tend to zero, leading again to an integrand equal to zero. Nevertheless, to be sure to eliminate all possibilities of divergence in the calculations when evaluating the integrand of Equation 4.6 at $r = R_c - a_G$, Pratt et al. (2001) suggested to simply evaluating the integral from 0 to $R_c - a_G - \xi$, where ξ is a very small number (0.0001 Å).

Modelling $\Delta \mu_w^{\beta - L, \alpha}$

Following Holder et al. (1980), the chemical potential difference between water in the hypothetical empty lattice and water in either the ice phase ($T \leq 273.15$ K) or the liquid phase ($T \geq 273.15$ K) can be expressed as:

$$
\begin{aligned}
\left(\frac{\Delta \mu_w^{\beta - L, \alpha}}{RT} \right)_{(T,P)} = & \left(\frac{\Delta \mu_w^{\beta - L, \alpha}}{RT} \right)_{(T_0, P_0)} - \int_{T_0}^{T} \frac{\Delta h_w^{\beta - L, \alpha}}{RT^2} dT \\
& + \int_{P_0}^{P} \frac{\Delta v_w^{\beta - L, \alpha}}{RT} dP - \ln(a_w^L)
\end{aligned}
\tag{4.13}
$$

where the reference conditions T_0 and P_0 are generally taken as $T_0 = 273.15$ K and $P_0 = 1$ bar. The temperature dependence of the enthalpy difference is given by:

$$
\Delta h_w^{\beta - L, \alpha} = \Delta h_w^{\beta - L, \alpha}(T_0) + \int_{T_0}^{T} \Delta C_p^{\beta - L, \alpha} dT
\tag{4.14}
$$

where the variation of the heat capacity is approximated by:

$$
\Delta C_p^{\beta - L, \alpha} = \Delta C_p^{\beta - L, \alpha}(T_0) + b^{\beta - L, \alpha}(T - T_0)
\tag{4.15}
$$

where $b^{\beta - L, \alpha}$ is a constant. The volume difference $\Delta v_w^{\beta - L, \alpha}$ is assumed to be independent of pressure. The last term of the second member of Equation 4.13 involves the activity of water a_w^L, which is defined by:

$$
a_w^L = \gamma_w \, x_w = \frac{f_w^L}{f_w^0}
\tag{4.16}
$$

where γ_w is the activity coefficient of water, x_w is the mole fraction of water in the liquid phase and f_w^L and f_w^0 are the water fugacities in the aqueous phase and in pure water, respectively. If we consider the liquid phase as ideal, the activity coefficient γ_w can be set to a fixed value of 1. The mole fraction of water is then estimated by determining the fraction of dissolved gas in the liquid phase: $x_w = 1 - x_G$. The latter is usually

small due to the low solubility of clathrate formers in water. For the ice phase, the activity of water is unity, making the term $\ln(a_w^L)$ in Equation 4.13 equal to zero. Thermodynamic reference parameters for sI and sII clathrates when $T \leq 273.15$ K are reported in Table 4.2.

Table 4.2: Thermodynamic reference properties for structure I and II clathrate hydrates: $T_0 = 273.15$ K, $P_0 = 1$ bar.

	Structure I	Structure II	Ref.
$\Delta\mu_w^{\beta-\alpha}$ (T_0,P_0) (J mol^{-1})[a]	1287	1068	Handa and Tse (1986)
$\Delta h_w^{\beta-\alpha}$ (T_0) (J mol^{-1})	931	764	Handa and Tse (1986)
$\Delta v_w^{\beta-\alpha}$ (T_0) (m^3 mol^{-1})	3.0×10^{-6}	3.4×10^{-6}	Anderson et al. (2005)
$\Delta C_p^{\beta-\alpha}$ (J mol^{-1} K^{-1})	$0.565 + 0.002\,(T - T_0)$		Holder et al. (1980)

[a] Superscripts/subscripts: w = water, β = empty clathrate lattice, α = ice phase.

Accurate values for the thermodynamic reference properties used in the statistical mechanical model of van der Waals and Platteeuw (1959) are essential. Unfortunately $\Delta\mu_w^0$ and Δh_w^0 have been found to take a wide range of values, due to the difficulties in determining these quantities experimentally, and have been used rather to fit experimental data than to make exact predictions (Cao et al., 2001; Herri and Chassefière, 2012).

Final expression

By combining Equations 4.2, 4.3 and 4.13, we obtain the expression that predicts the equilibrium pressure of clathrates at a given temperature and vice versa:

$$
\begin{aligned}
-RT\sum_i \nu_i \ln(1 - \sum_G \theta_{G,i}) =& T\,\frac{\Delta\mu_w^{\beta-L,\alpha}}{T_0} - T\int_{T_0}^{T}\frac{\Delta h_w^{\beta-L,\alpha}}{T^2}dT \\
&+ \int_{P_0}^{P}\Delta v_w^{\beta-L,\alpha}dP - RT\ln\left(a_w^L\right)
\end{aligned}
\tag{4.17}
$$

A typical algorithm to find the pressure formation of clathrates from the initial mole fractions of different components in a given gas mixture at a given temperature is shown in Fig. 4.2. First, the Langmuir constants for each component in all cavities of both clathrate structures I and II are calculated via Equation 4.6. According to the input temperature, a first estimation of the formation pressure is made and used to determine the fugacity of every component in the gaseous phase. The chemical potential differences are then calculated (Equations 4.3 and 4.13) and

compared. If their values are close enough, the estimated pressure was the good one. Otherwise, the pressure is adjusted and the fugacity, $\Delta\mu_w^{\beta-H}$ and $\Delta\mu_w^{\beta-L,\alpha}$ are calculated again with this new pressure. This procedure is repeated until the chemical potential differences correspond. Once the formation pressure is found for sI and sII clathrates, the structure that actually crystallizes is considered to have the lowest formation pressure. This algorithm is commonly used in programs predicting the thermodynamics of stable clathrate structures such as CSMHYD (Colorado School of Mines, HYDrates), which has been developed to study clathrate hydrates on Earth (Sloan and Koh, 2007). This program is executable and allows the user to enter the number, nature and mole fractions of the different components in the gas phase. Then, it computes the equilibrium pressure at the temperature specified by the user, with or without inhibitor(s) in the aqueous phase (a salinity increase results in a decrease of water activity). In addition, standard outputs include equilibrium phases and their compositions, crystal structure and fractional occupancy.
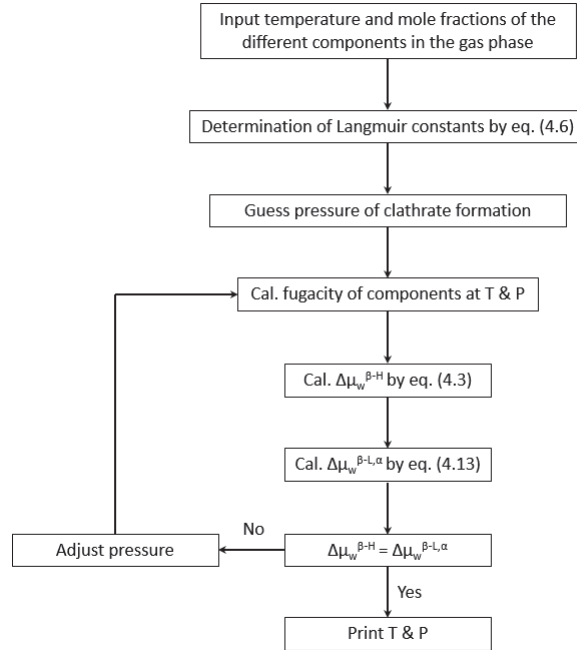

Figure 4.2: Typical algorithm to determine formation conditions of clathrate hydrates with the model of van der Waals and Platteeuw (1959).

Although of great precision, CSMHYD is not suitable to the temperature conditions prevailing at high latitude on Mars because the method

does not converge for conditions far from reference conditions ($T_0 = 273.15$ K, $P_0 = 1$ bar). Consequently, Chastain and Chevrier (2007), who investigated composition and stability of binary CO_2-CH_4 clathrates in the martian subsurface using this program, were not able to calculate the composition of clathrate hydrates formed below 173K. Moreover, the CSMHYD program has a limited list of available species and does not allow to consider all the components of the martian atmosphere such as argon. Thomas et al. (2009) determined the composition of mixed CO_2-CH_4-N_2-Ar clathrates as a function of temperature and initial gas phase composition using a hybrid model based on the work of van der Waals and Platteeuw (1959) and on available experimental dissociation curves. This approach allows to include minor compounds in the martian atmosphere and does not suffer from low temperature restriction. As mentioned previously, Herri and Chassefière (2012) used the same kind of method fitting the model of van der Waals and Platteeuw (1959) and comparing the deviation from experimental data at low temperature. They implemented in their software called GasHydDyn (Java language) a minimization algorithm to determine Kihara and reference parameters from experimental data base (pressure, temperature, gas and clathrate compositions) or inversely. In each case, clathrate compositions have been determined at the dissociation pressure.

In this study, we follow an approach similar to Thomas et al. (2009) where the dissociation pressure P_{mix}^{diss} of a multiple guest clathrate is calculated from the dissociation pressures of simple guest clathrates as (Lipenkov and Istomin, 2001):

$$P_{mix}^{diss} = \left(\sum_G \frac{x_G}{P_G^{diss}} \right)^{-1} \tag{4.18}$$

where x_G is the molar fraction of species G in the initial gas phase. The dissociation pressure P_G^{diss} of a simple clathrate of guest species G follows an Arrhenius law (Miller, 1961):

$$\log(P_G^{diss}) = A + \frac{B}{T} \tag{4.19}$$

where P_G^{diss} is expressed in Pa and T is the temperature in K. The constants A and B fit to the experimental data presented in Fig. 3.7 and are listed in Table 4.3. Most of these constants are valid below the quadruple point Q_1 of clathrates (I-H-V equilibrium curve) as this is the stability region investigated in this work. For H_2 clathrate, given the lack and considerable dispersion in the experimental data below the quadruple point (T = 263.85 K), we decided to study the influence of H_2

trapping in methane clathrate only over a temperature range from 263.85 K to 273.15 K. Experimental dissociation pressures obtained between Q_1 and 269.15 K for the system $H_2 + H_2O$ (Chapoy et al., 2010) have thus been fitted to obtain A and B. Moreover, as the base of clathrate stability zone is investigated for simple clathrate of methane, A and B above Q_1 have been determined as well for CH_4. Fig. 4.3 compares the dissociation pressure computed with this approach and those obtained with CSMHYD and GasHydDyn for a mixed clathrate formed from an initial gas phase with 50% of CH_4, 30% of CO_2 and 20% of N_2.

Table 4.3: Parameters A and B (K) required in Equation 4.19 to calculate the dissociation pressure of simple clathrates.

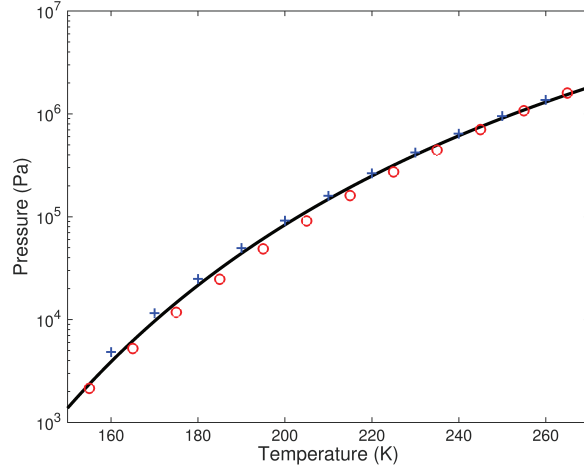| Molecule	A	B (K)	T range
CH_4	9.65	-895.9	$\leq Q_1$
CH_4	21.46	-4124.4	$\geq Q_1$
CO_2	10.13	-1116.9	$\leq Q_1$
N_2	9.74	-702.57	$\leq Q_1$
Ar	9.24	-630.86	$\leq Q_1$
H_2	19.70	-3080.7	$\geq Q_1$

Figure 4.3: Dissociation pressure as a function of temperature for a mixed clathrate formed from an initial gas phase with 50% of CH_4, 30% of CO_2 and 20% of N_2. The calculations were done with the approach described above (black curve), the CSMHYD program (crosses) and the GasHydDyn software (circles).

Equation 4.18 gives a very good estimation of the dissociation pressure. It can be seen in Fig. 4.3 that this method provides similar results to CSMHYD and GasHydDyn at temperature close to 270 K. At lower temperature, the pressure slightly differs from that predicted by the two stability models, which also deviate from each other. However, P_{mix}^{diss} remains in the region delimited by CSMHYD and GasHydDyn, showing the validity of the method. Once the equilibrium pressure is known, the relative abundance of a species G in a clathrate hydrate is given by:

$$x_G^H = \frac{b_s \theta_{G,s} + b_l \theta_{G,l}}{b_s \sum_J \theta_{J,s} + b_l \sum_J \theta_{J,l}} \qquad (4.20)$$

where the sum at the denominator takes into account all the species in the gas phase and b_s and b_l are the number of small and large cavities per unit cell respectively. The occupancy fraction $\theta_{G,i}$ is calculated via Equation 4.4 where the fugacities and Langmuir constants are determined using the Peng-Robinson equation of state and the Equation 4.6, respectively. Although the approach based on Equation 4.18 does not predict which clathrate structure will preferably be formed and makes the composition calculations for both structures I and II necessary for each application, it is quite simple to be implemented in our subsurface model, described in the next section.

Finally, it is important to note that the assumed spherical symmetry of the interaction potential can be questionable and may not accurately describe the interaction between enclathrated and water molecules. As a result, it may lead to the evaluation of erroneous relative abundances of gas species in clathrate hydrates. Some works have thus focused on the evaluation of proper guest-clathrate interaction potentials with parameters directly deduced from ab initio quantum mechanical calculations (Klauda and Sandler, 2002, 2003; Sun and Duan, 2005). Recently, Lakhlifi et al. (2015) proposed a van 't Hoff law expression of Langmuir constants where parameters have been determined using a pairwise atom-atom Lennard-Jones and a site-site electrostatic potentials to calculate the guest-clathrate interaction in an anisotropic environment:

$$C_{G,i}(T) = U_{G,i} \exp\left(\frac{V_{G,i}}{T}\right) \qquad (4.21)$$

where U (Pa^{-1}) and V (K) are constant parameters listed in Table 4.4. The model of Lakhlifi et al. (2015) takes into account all the external degrees of freedom of the guest and water molecules and considers explicitly the effect of water molecules beyond the trapping cage: calculations were made over the first four and three hydration shells for sI and sII clathrates, respectively, to ensure a good convergence of the results

(Thomas et al., 2010). Equation 4.21 can be applied in the temperature range 50 K - 300 K and we therefore use it to investigate clathrate composition and compare results obtained with Equation 4.6. Langmuir constants computed for sI methane clathrate with both methods are presented in Fig. 4.4. Calculations using the Kihara potential show similar Langmuir constants in both types of cage, while the van 't Hoff law expression suggests a more efficient enclathration of CH_4 in the large cage of structure I as its Langmuir constant is higher than in the small cavity at the same temperature.

Table 4.4: Parameters $U_{G,i}$ (Pa^{-1}) and $V_{G,i}$ (K) used in Equation 4.21 to calculate the Langmuir constants for simple guest clathrate hydrates. These parameters are derived from Lakhlifi et al. (2015).

Structure type-cage size	sI-small cage	sI-large cage	sII-small cage	sII-large cage
Guest species G	$U_{G,i}$	$U_{G,i}$	$U_{G,i}$	$U_{G,i}$
	$V_{G,i}$	$V_{G,i}$	$V_{G,i}$	$V_{G,i}$
CH_4	8.3453×10^{-10}	116.6313×10^{-10}	5.4792×10^{-10}	829.8039×10^{-10}
	2901.747	2959.901	2546.660	2629.194
CO_2	7.7765×10^{-12}	520.5579×10^{-12}	7.9970×10^{-12}	$6907.0012 \times 10^{-12}$
	2976.629	4674.690	2277.757	3370.363
N_2	3.9496×10^{-10}	25.6897×10^{-10}	4.8836×10^{-10}	201.3238×10^{-10}
	2869.400	2680.372	2679.423	2226.480
Ar	1.5210×10^{-10}	7.7829×10^{-10}	1.0456×10^{-10}	2.4531×10^{-10}
	2961.545	2521.758	2977.025	2195.964
H_2	4.7301×10^{-9}	16.0695×10^{-9}	5.5295×10^{-9}	64.0074×10^{-9}
	1265.757	1515.721	1203.620	873.259

4.3 Thermal model

4.3.1 Determination of surface temperature on slopes

This section describes the model used to determine surface temperature including implementation of slopes, which is similar to Schorghofer and Edgett (2006). Indeed, local slopes considerably alter surface and subsurface temperatures due to the difference in sunlight incidence and outgoing radiation and can therefore affect water ice and clathrate distribution in the soil. The atmospheric component of the model is pretty simple. However, we are mainly interested here in the impact of slopes on thermal conditions.

The heat balance on the surface includes incoming solar radiation Q, conduction into the soil, black body radiation by the surface and latent heat of CO_2:

$$Q(\alpha) + k \left(\frac{\partial T}{\partial z}\right)_{z=0} = \epsilon \sigma T^4 + L_{CO_2} \frac{\partial m_{CO_2}}{\partial t} \qquad (4.22)$$
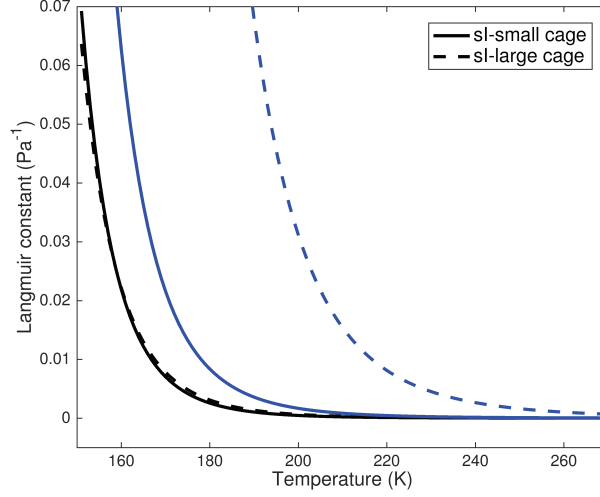
Figure 4.4: Langmuir constants calculated for sI methane clathrate with Equations 4.6 (black curves) and 4.21 (blue curves) as a function of temperature.

where α is the slope angle, ϵ the emissivity (assumed to be 1; Kieffer et al. (1977)), σ the Stefan-Boltzmann constant, L_{CO_2} the latent heat of carbon dioxide ($L_{CO_2} = 590$ kJ kg^{-1}) and m_{CO_2} the areal mass density of CO_2. The incoming flux Q is composed of four terms, which are represented in Fig. 4.5:

$$Q(\alpha) = Q_{\text{solar}}(\alpha) + Q_{\text{IR}}(\alpha) + Q_{\text{scat}}(\alpha) + Q_{\text{land}}(\alpha) \qquad (4.23)$$

where Q_{solar} is the direct solar insolation, Q_{IR} is the thermal infrared emission from the atmosphere, Q_{scat} is the scattered light and Q_{land} is the thermal radiation received from other surfaces in the field of view of the sloped surface.
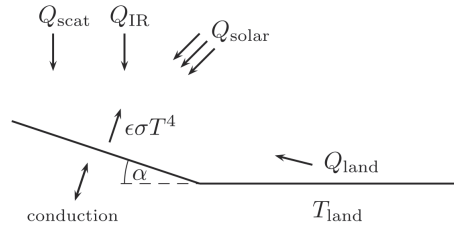

Figure 4.5: Contributions to the heat balance on a frost free surface with a slope angle α and a surface temperature T (Aharonson and Schorghofer, 2006).

The primary effect of a slope is to modify the incidence angle of direct sunlight. The angle θ of the Sun above a sloped surface is given by:

$$\sin\theta = \cos\alpha\sin\beta - \sin\alpha\cos\beta\cos(\Delta a) \quad (4.24)$$

where Δa is the difference between the azimuth of the Sun and the azimuth of the topographic gradient and β the elevation of the Sun, expressed by:

$$\sin\beta = \cos\phi\cos\delta\cos h + \sin\phi\sin\delta \quad (4.25)$$

where ϕ is the geographic latitude, δ the declination of the Sun and h the hour angle. When $\sin\beta < 0$ or $\sin\theta < 0$, the Sun is assumed to be below the horizon and Q_{solar} is therefore set to 0. Otherwise, its value is given by:

$$Q_{\text{solar}} = \frac{S_0}{R^2}(1-A)(1-f)^{1/\max(\sin\beta,0.04)}\sin\theta \quad (4.26)$$

where S_0 is the solar constant (at 1 AU), A is the albedo and the factor f is due to the extinction of the atmosphere ($f = f_{\text{IR}} + f_{\text{scat}}$). The term $1/\max(\sin\beta, 0.04)$ takes into account the path length through the atmosphere. The distance from the Sun R in AU is calculated following Allison and McEwen (2000):

$$\begin{aligned} R = 1.5236\,(1.00436 &- 0.09309\cos M - 0.00436\cos(2M) \\ &- 0.00031\cos(3M)) \end{aligned} \quad (4.27)$$

where M is the mean anomaly. The thermal infrared emission is evaluated as a fraction $f_{\text{IR}} = 0.04$ (Kieffer et al., 1977) of noontime insolation and is kept constant during the day:

$$Q_{\text{IR}} = f_{\text{IR}}\frac{S_0}{R^2}\cos^2\left(\frac{\alpha}{2}\right)\sin\beta_{\text{noon}} \quad (4.28)$$

In addition, when $\sin\beta > 0$, the scattered light term is approximated by:

$$Q_{\text{scat}} = \frac{1}{2}f_{\text{scat}}\frac{S_0}{R^2}\cos^2\left(\frac{\alpha}{2}\right) \quad (4.29)$$

where half of Q_{scat} is considered to be lost to space and $f_{\text{scat}} = 0.02$ (Schorghofer and Edgett, 2006). Finally, the last contribution to Q is given by:

$$Q_{\text{land}} = \sin^2\left(\frac{\alpha}{2}\right)\epsilon_{\text{land}}\sigma T_{\text{land}}^4 \quad (4.30)$$

A default value of 0.25 (Kieffer et al., 1977) is chosen for albedo
when no CO_2 covers the surface. The Equation 4.22 is then solved for
the surface temperature using the Newton-Raphson method and when
the temperature falls below the sublimation temperature of CO_2 (147 K
in the northern hemisphere, 143 K in the southern hemisphere; Aharon-
son and Schorghofer (2006)), carbon dioxide begins to accumulate on the
surface and albedo is changed accordingly ($A = 0.65$). The surface tem-
perature remains at a constant value (147 K or 143 K depending on the
location) until all the CO_2 finally sublimates away. During this time, the
surface heat balance is solved for m_{CO_2} to determine the mass of carbon
dioxide that either sublimates or condenses at each time step. Fig. 4.6
shows examples of surface temperature obtained with slope implementa-
tion. As expected, the surface temperature on an equator-facing (resp.
pole-facing) slope is higher (resp. lower) than on a flat floor. For the
right panel, model inputs have been chosen similar to Aharonson and
Schorghofer (2006). Their results for the variation of the mean surface
temperature with the slope angle are comparable to ours showing the
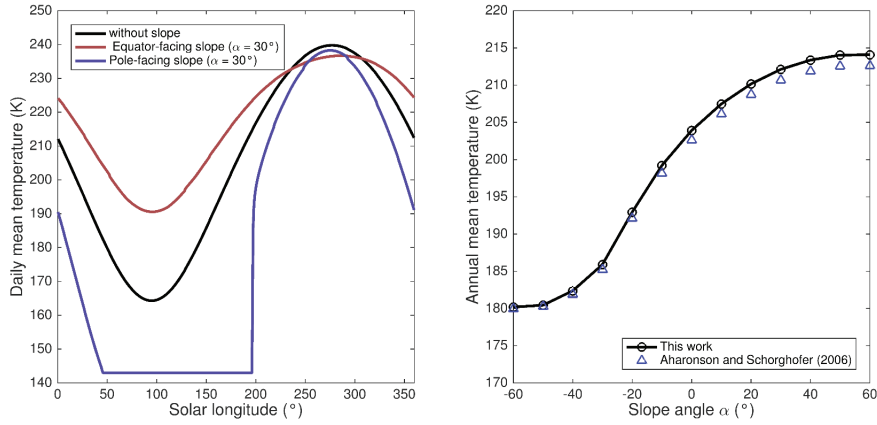proper implementation of slopes in our model.

Figure 4.6: (Left) Daily average surface temperature at 40°S as a function of
solar longitude. Calculations were made without slope (black curve), with an
equator-facing slope of 30°(red curve) and with a pole-facing slope of 30°(blue
curve). The albedo of the surface is $A = 0.25$ and the thermal inertia $I = 250$
J m^{-2} K^{-1} s$^{-1/2}$. (Right) Annual mean surface temperature as a function of
slope at 35°N. Equator-facing slopes are shown as positive and pole-facing as
negative. Albedo and thermal inertia have been taken similar to Aharonson
and Schorghofer (2006) ($A = 0.3$ and $I = 150$ J m^{-2} K^{-1} s$^{-1/2}$).

4.3.2 Subsurface temperature

A one-dimensional diffusion equation for subsurface temperature with depth dependent thermal conductivity, density and specific heat is solved with a semi-implicit (unconditionally stable) Crank-Nicolson scheme on a grid with variable spacing:

$$\rho(z)c(z)\frac{\partial T(z,t)}{\partial t} = \frac{\partial}{\partial z}\left(k(z)\frac{\partial T(z,t)}{\partial z}\right) + \rho(z)H \qquad (4.31)$$

where ρ is density, c is specific heat capacity, T is temperature, z is vertical coordinate, t is time, k is thermal conductivity and H is radiogenic heat production. The latter is set to a constant value (5×10^{-11} W kg^{-1}) assuming a vertically homogeneous distribution of radiogenic heat-producing elements in the planet's crust (Hahn et al., 2011). Each subsurface layer can have specific thermal properties of density, heat capacity and thermal conductivity assigned to them. Fig. 4.7 shows daily average temperature profiles calculated at regular intervals over a martian year for a homogeneous dry soil and a layered subsurface. For the latter, thermal properties are changed below 50 cm deep to correspond to those of ice-cemented soil. It can be seen that the amplitude of temperature oscillations is greater in dry soil than in ice-cemented soil. However, these oscillations reach a more important depth in the soil saturated with ice.

In our simulations to determine global maps of the top of the clathrate stability zone (TCSZ), the subsurface model is divided in two layers. The thermal properties of the upper layer are set to fit with the thermal inertia derived from Mars Global Surveyor Thermal Emission Spectrometer observations (Putzig and Mellon, 2007). Accordingly, the regolith bulk density ρ_b (kg m^{-3}) of this layer is determined as a function of thermal inertia I (J m^{-2} K^{-1} s$^{-1/2}$) following the empirical relation from Mellon and Jakosky (1993):

$$\rho_b = 150 + 100\sqrt{34.2 + 0.714I} \qquad (4.32)$$

with a maximum value assumed to be 2500 kg m^{-3}. The specific heat capacity c is set to 800 J kg^{-1} K^{-1} and the thermal conductivity k is then determined using $k = I^2/(\rho_b c)$. The properties of the lower layer depend on the latitude of the studied area. Between 50°N and 50°S, the top of the lower layer is set to 1 m deep and its thermal properties are representative of dry basalt. Northward of 50°N and southward of 50°S, the lower layer starts at 50 cm deep and has thermal properties representative of ice-saturated soil. The compression of pore spaces with depth is modelled following Clifford (1993):
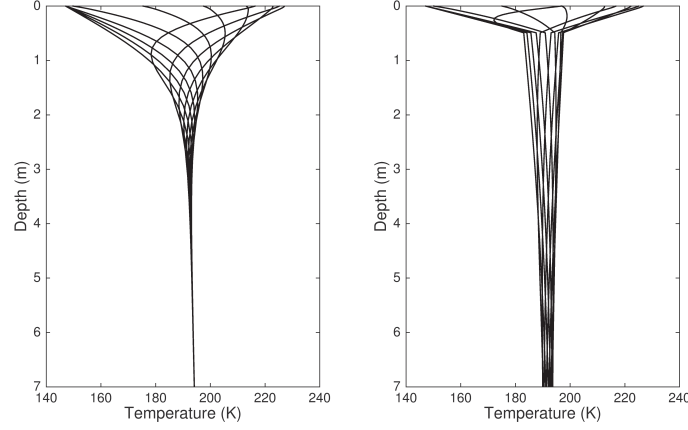
Figure 4.7: Example subsurface temperature profiles for a homogeneous dry soil ($I = 250$ J m^{-2} K^{-1} s$^{-1/2}$)(left) and a layered subsurface (right) at a latitude of 55°N. Each curve is a diurnal average temperature profile calculated at regular intervals for a full martian year. For the layered case, thermal properties are changed below 50 cm deep to correspond to those of ice-cemented soil ($I = 2290$ J m^{-2} K^{-1} s$^{-1/2}$). The heat flow is assumed equal to 19 mW m^{-2}.

$$\Phi(z) = \Phi_0 \exp(-z/K_0) \qquad (4.33)$$

where Φ_0 is the surface porosity (40%), z is the depth and K_0 is the porosity decay constant (~ 2.82 km). The variation of the volumetric heat capacity and thermal conductivity with depth is then given by:

$$\rho c(z) = (1 - \Phi(z))\rho_{\mathrm{dry}}c_{\mathrm{dry}} + \Phi(z)\rho_{\mathrm{ice}}c_{\mathrm{ice}} \qquad (4.34)$$

$$k(z) = k_{\mathrm{dry}}^{(1-\Phi(z))}k_{\mathrm{ice}}^{(\Phi(z))} \qquad (4.35)$$

where properties of water ice and basalt are referred to in Table 4.5.

Table 4.5: Typical thermophysical properties of geological materials used in this study.

	k (W m^{-1} K^{-1})	ρ (kg m^{-3})	c (J kg^{-1} K^{-1})	I (J m^{-2} K^{-1} s$^{-1/2}$)
Water ice	2.8	920	1960	2247
Basalt	2	3000	800	2190
Ice-saturated soil	2.5	2018	1040	2290
Dry unconsolidated soil	0.045	1650	800	244

The changes in surface temperature and pressure in latitude and longitude over the martian year are given by the Mars Climate Database v5.2 ("Climatology" scenario, average solar EUV conditions) (Forget et al., 1999; Millour et al., 2015). The present-day heat flow variations across the martian surface are taken from the model of Parro et al. (2017) that provides a surface heat flow varying between 14 and 25 mW m^{-2} with an average value of 19 mW m^{-2}.

Finally, the pressure in pore spaces that controls stability of methane clathrate hydrates in subsurface has two limiting cases: lithostatic and atmospheric pressure. Assuming isolated porosity, the local confining pressure is equal to the lithostatic pressure:

$$P(z) = P_s + \rho g z \qquad (4.36)$$

where P is lithostatic pressure at depth z, P_s is surface pressure, ρ is density of overburden and g is average gravity on Mars surface (3.72 m s^{-2}). Alternatively, if the pore spaces are open, the gas phase pressure in subsurface is much smaller than previously and is given by the barometric equation:

$$P(z) = P_s \exp\left(\frac{gM}{RT_s} z\right) \qquad (4.37)$$

where P is gas phase pressure at depth z, M is molecular weight of the atmosphere (44 g/mol), R is ideal gas constant and T_s is surface temperature. However, the real pore pressure profile is generally more complex with an intermediate value between the lithostatic and the depth-ajusted barometric pressure depending on how pores are connected and their saturation state (Max and Clifford, 2000).

Scenarios for Early Mars

These scenarios are used in the next chapter when investigating the evolution of the martian cryosphere with time. The mean surface temperature of Early Mars remain uncertain and two different scenarios are therefore adopted. In the first one, the mean surface temperature at the equator 4 Gyr ago is set to 273.15 K, which assumes a warmer early Mars with some periods of the year where temperatures regularly exceed the freezing point of water. In this scenario represented in Fig. 4.8a (Haberle, 1998), mean surface temperature decreases rapidly during the first billion years to a value about 235 K. Then, it declines smoothly until present time to reach 220 K, the current mean equatorial temperature. In the second scenario, the mean surface temperature is set to a constant value equal to 220 K. The evolution of the surface heat flow is determined by

curve fitting to the model of Grott and Breuer (2010) and is represented in Fig. 4.8b. Grott and Breuer (2010) obtained similar results to Hauck and Phillips (2002) with values of the surface heat flow around 60 mW m^{-2} at 3.5 Gyr and about 20 mW m^{-2} today. The latter number is consistent with the present average value of 19 mW m^{-2} found by Parro et al. (2017). Surface abundances of K and Th have been measured by the Gamma Ray Spectrometer on board the 2001 Mars Odyssey spacecraft (Taylor et al., 2006) while U abundances have been determined assuming a Th/U ratio of 3.8 (Hahn et al., 2011). Using the surface average heat-producing elements abundances (0.18, 0.69 and 3652 ppm for U, Th, and K respectively (Ruiz et al., 2011)), the crustal heat production is determined and its evolution through time is shown in Fig.4. Its average value varies between 20×10^{-11} W kg^{-1} at 4 Gyr and 5×10^{-11} W kg^{-1} at present day (Hahn et al., 2011).
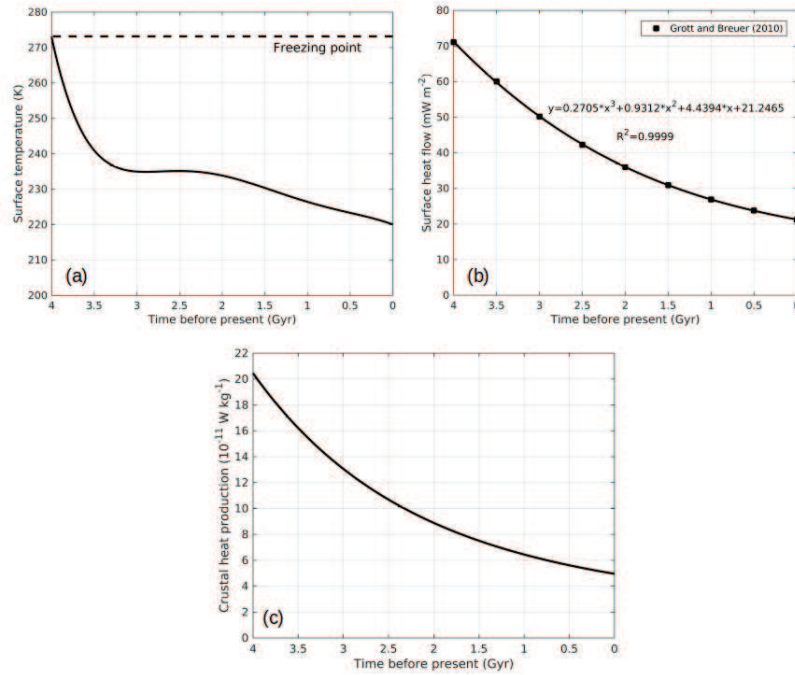

Figure 4.8: Scenarios for the evolution of (a) martian surface temperature at the equator (warm scenario) (Haberle, 1998), (b) martian surface heat flow (Grott and Breuer, 2010) and (c) crustal heat production used in the present study.

4.4 Transport of gases in porous media

The second part of this chapter describes the diffusive-adsorptive model used to study methane and water vapor transport from shallow sources through the porous subsurface of Mars. Advection is also briefly discussed although we did not investigate this process.

4.4.1 Mass transfer versus mass transport

During CH_4 and H_2O gases transport through the martian soil, some of the moving gases will adsorb onto rock surfaces and H_2O vapor will also condense into ice. Mass transfer refers to transfer of mass or partitioning of soil gases between the solid and gas phases and therefore slows up their migration through the subsurface. For water vapor transport, it is described as:

$$\sigma = \phi \left(1 - f_i\right) \rho_G + \phi \rho_i + \rho_a \qquad (4.38)$$

where σ is the total water content (kg m^{-3}), ϕ is the regolith porosity, f_i is the volumetric fraction to which pore spaces are filled with ice, ρ_G is the vapor density in the void space (not occupied by regolith or water ice), ρ_i is the ice density in pore space and ρ_a is the density of adsorbed water. For methane transport, Equation 4.38 is reduced to:

$$\sigma = \phi \rho_G + \rho_a \qquad (4.39)$$

4.4.2 Mechanisms of gas transport

The important parameters to determine which gas transport regime is dominant include the mean free path (the average distance a gas molecule travels before colliding with another), the pore size and the particle size. Following this, gas transport through porous media can be divided in different mechanisms (Mason and Malinauskas, 1983):

- Free molecule or Knudsen flow occurs when the pore radius is less than one tenth of the gas mean free path, and molecule-wall collisions dominate.

- Viscous or advective flow, in which the gas acts as a continuum fluid under the influence of a pressure gradient. Advection is dominant when the gas mean free path is much smaller than the pore radius and the particule radius resulting in molecule-molecule collisions being dominant.

- Ordinary or molecular diffusion refers to the relative motion of the different gas species under the influence of concentration gradients, temperature gradients (thermal diffusion), pressure gradients (pressure diffusion) or external forces such as electric or magnetic field (forced diffusion). In this regime, the pore radius is larger than $10\times$ the gas mean free path and collisions between gas molecules dominate.

- Surface flow or diffusion in which molecules move along a solid surface in an adsorbed layer.

Surface diffusion is generally not significant (Scanlon et al., 2002) and is thus not taken into account in this work. Pressure diffusion and thermal diffusion are also neglected as their contribution is rather small compared to molecular diffusion (concentration gradients) and Knudsen diffusion, which are normally considered to be the most important diffusive processes in soils (Thorstenson and Pollock, 1989a,b). Moreover, the diffusive model is applied with near-surface sources and pressure diffusion is usually negligible at depths of less than 100 m (Amali and Rolston, 1993).

The total molar flux N^T of a gas mixture in a porous medium is given by the sum of the flux resulting from diffusion N^D and the advective flux N^V. For the ith species, it is written as:

$$N_i^T = N_i^D + N_i^V \tag{4.40}$$

4.4.3   Advective flux

If a total pressure gradient exists in the subsurface, gases will be transported from regions of higher to those of lower pressure. Advective flow does not lead to the separation of the different species in the gas mixture, which are thus all transported at the same rate. The molar viscous flux of gas component i satisfies the relation:

$$N_i^V = y_i N^V \tag{4.41}$$

where y_i is the mole fraction of component i and N^V is represented by Darcy's law:

$$N^V = -c_T \frac{k_G}{\mu_G} \left(\frac{\partial P}{\partial z} - \rho_G g \right) \tag{4.42}$$

where c_T is the total molar concentration, k_G is the gas permeability of the porous medium, μ_G is the gas-phase viscosity, ρ_G is the gas density, g

is the gravitational acceleration and z is the vertical coordinate increasing downward. The first term in parentheses is the driving force due to pressure and the second term is the driving force due to gravity. From Equation 4.42, it can be seen that the main driving force for advective flow is the pressure gradient, while the resistance to flow is caused by the gas viscosity.

When the pore size reduces as a result of decreasing grain size, the flow regime changes from advective flux to viscous slip flux (Klinkenberg effect) to Knudsen diffusive flux. Klinkenberg effect occurs in the transition flow regime when the mean free path of the gas molecules becomes approximately the same as the pore radius and results in a nonzero gas velocity at the pore wall and in underestimation of gas flux by Darcy's law. Indeed, according to Equation 4.42, the molar flux should decrease as the average pressure is reduced. However, the flux reaches a minimum value at low pressures and then increases with decreasing pressure due to slip flow (Ho and Webb, 2006). The permeability k_G actually depends on the pressure and has been evaluated by Klinkenberg et al. (1941) that derived the following expression:

$$k_G = k_l \left(1 + \frac{b_i}{\bar{P}} \right) \tag{4.43}$$

where k_l is the permeability at infinite pressure when the gas behaves as a liquid, b_i is a constant function of the porous medium and the gas i and $\bar{P}$ is the mean pressure. At large mean pressure, liquid and gas permeabilities are similar. As the average pressure decreases, the two permeabilities differ from each other and gas slippage is enhanced.

4.4.4 Molecular diffusive flux

Molecular diffusion occurs when a concentration or mole fraction gradient exists and implies the counterdiffusion of equimolar pairs of gases in pores whose size is much larger than that of the mean free path of the gas species. This mechanism therefore takes place even under isothermal and isobaric conditions and is considered to be "segregative" because it results in separation of the different component gases. Fick's first law is commonly used to describe the molar diffusive flux of gas i in gas j:

$$N_i^F = -D_{ij} c_T \frac{\partial y_i}{\partial z} \tag{4.44}$$

where $D_{ij} = D_{ji}$ (Bird et al., 2007) is the molecular diffusion coefficient that depends on temperature, pressure and the properties of the two gases. Note that Fick's law excludes the effects of Knudsen diffusion and

nonequimolar diffusion and its adaptation for use in porous media will be discussed later.

4.4.5   Bulk diffusive flux

In general, equimolar counterdiffusion is rare in porous media. Bulk diffusion includes molecular and nonequimolar diffusion, for which gas components have different molecular weights. Lighter molecules diffuse faster than heavier gas molecules, which gives rise to a pressure gradient that will move the gas phase in the direction opposite to the flow of lighter molecules. The resulting flux (nonsegregative) is diffusive and is called nonequimolar flux or diffusive slip flux (Cunningham and Williams, 1980). The molar bulk diffusive flux of gas component i can be written as:

$$N_i^D = N_i^F + y_i \sum_{j=1}^{n} N_j^D \tag{4.45}$$

where n is the number of gas components and $y_i \sum_{j=1}^{n} N_j^D$ is the nonequimolar flux.

4.4.6   Knudsen diffusive flux

As explained earlier, the Knudsen diffusion becomes important when the gas mean free path is much larger than the pore radius. In the Knudsen region, the molar flux of component i is given by:

$$N_i^D = -D_{iK} c_T \frac{\partial y_i}{\partial z} \tag{4.46}$$

The Knudsen diffusion coefficient D_{iK} depends on pore geometry and is defined as:

$$D_{iK} = \frac{2}{3} r \sqrt{\frac{8 k_B T}{\pi m_i}} \tag{4.47}$$

where r is the pore radius and m_i the molecular mass of the gas component i. It is important to note that the presence of water ice in pore spaces will affect the diffusion by reducing the pore size. In a regolith with an initial large pore diameter, a transition will take place in the flow regime from molecular-dominated to Knudsen-dominated diffusion as the open pores become smaller.

4.4.7 Effective diffusion coefficient

In the transition region, when the gas mean free path is about the same order of magnitude as the pore size, both molecular and Knudsen diffusion have to be taken into account. In this flow regime, an effective diffusion coefficient D_{eff} is commonly defined according to the Bosanquet interpolation formula:

$$\frac{1}{D_{\text{eff}}} = \frac{1}{D_{12}} + \frac{1}{D_{1K}} \qquad (4.48)$$

Fig. 4.9 represents the evolution of the effective diffusion coefficient for water vapour as a function of pore radius. The Knudsen diffusion coefficient has been calculated with Equation 4.47, while the molecular diffusion coefficient has been determined following the expression given by Wallace and Sagan (1979) for H_2O diffusing through an atmosphere of CO_2 in martian conditions:

$$D_{H_2O-CO_2} = (0.1654\text{cm}^2\text{ s}^{-1}) \left(\frac{T}{273.15\text{K}}\right)^{3/2} \left(\frac{1013\text{mbar}}{P}\right) \qquad (4.49)$$
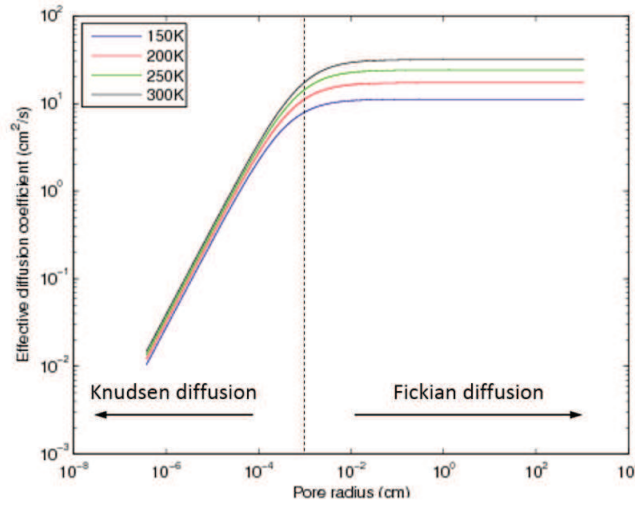

Figure 4.9: The effective diffusion coefficient for water vapour as a function of pore radius. Transport ranges from Knudsen to normal diffusion.

At martian pressures, the mean free path of CH_4 and H_2O molecules is $\sim 10\ \mu$m (Meslin et al., 2011) and 7-9 μm (Hudson, 2008), respectively.

These values are probably of the same order of magnitude as the mean pore size, which we assumed equal to 10 μm in the rest of this work.

Finally, the change in diffusion coefficient from free-gas to porous-media conditions is described by the ratio between the porosity Φ and the tortuosity τ, often called the obstruction factor:

$$D_{\text{porous media}} = \frac{\Phi}{\tau} D_{\text{eff}} \tag{4.50}$$

where the porosity ($\Phi < 1$) takes into account the limited pore cross section, while the tortuosity ($\tau > 1$) accounts for increased path length and dead ends in the porous subsurface.

4.4.8   Adsorption

The main parameters that control adsorption are the partial pressure of gas, temperature and nature of the soil material. Adsorption of water in the martian subsurface retards the ice formation since it separates water in a supplementary phase. The Langmuir isotherm that is usually used to describe adsorption of gases onto surfaces is given by:

$$\theta_{\text{eq}} = \frac{k_{\text{eq}}P}{1 + k_{\text{eq}}P} \tag{4.51}$$

where θ_{eq} is the fractional coverage of the monolayer at equilibrium, P is the partial pressure of gas and k_{eq} is the equilibrium rate constant, which describes the ratio between the adsorption rate constant and the desorption rate constant. Equation 4.51 is analogous to Equation 4.4 that determines the occupancy fraction in clathrate hydrates as a function of the Langmuir constant. The mass of adsorbed gas m_a (in kg kg^{-1}) is then expressed as:

$$m_a = \theta A_s m_{\text{ML}} \tag{4.52}$$

where A_s is the specific surface area of the regolith and m_{ML} is the mass per unit surface area of a single adsorbed monolayer of gas. By multiplying m_a by the bulk density of the regolith, we can obtain the value for ρ_a in Equation 4.38.

In Equation 4.51, adsorption is supposed instantaneous but a time lag exists to reach equilibrium, as represented in Fig. 4.10 for water vapor, due to the intrinsic kinetics of the adsorption process. The variation of the surface coverage θ as a function of time is given by (Zent et al., 2001):

$$\frac{d\theta}{dt} = k_a(1 - \theta) - k_d\theta \tag{4.53}$$

where k_a and k_d are the adsorption and desorption rate constants respectively. Solving this equation with the initial condition $\theta_{t=0} = 0$ gives:

$$\theta = \frac{k_a}{k_a + k_d}(1 - e^{-(k_a+k_d)t}) \tag{4.54}$$
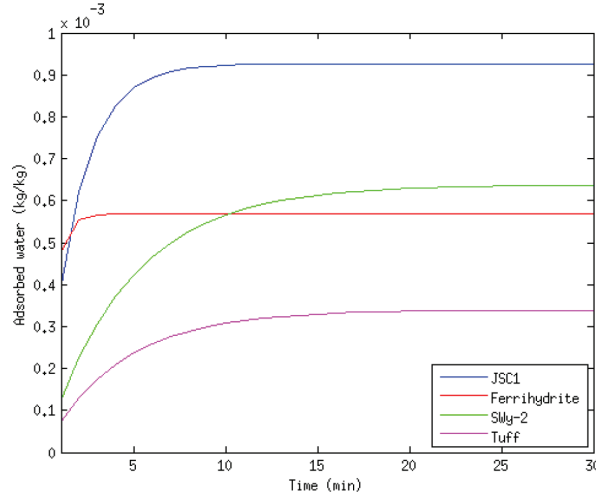

Figure 4.10: The amount of adsorbed water as a function of time for different samples at 243 K and 0.1 Pa. Kinetic constants and specific surface areas are taken from Beck et al. (2010) and Pommerol et al. (2009) respectively.

4.4.9 Gas transport models

Stefan-Maxwell equations

The Stefan-Maxwell equations are an extension of Fick's law for multicomponent gas mixtures and are given by:

$$\sum_{j=1, j\neq i}^{n} \frac{y_j N_i^D - y_i N_j^D}{D_{ij}} = -c_T \frac{dy_i}{dz} \tag{4.55}$$

These equations are available for diffusion in the bulk region only as they exclude Knudsen diffusion. The description of combined (diffusion and advection) transport of multicomponent gas mixtures is given by two models: the Dusty Gas Model (Mason and Malinauskas, 1983) and the Mean Transport Pore Model (see e.g. Arnošt and Schneider (1995)).

Dusty Gas Model (DGM)

The Dusty Gas Model (Mason and Malinauskas, 1983) is based on the full Chapman Enskog kinetic theory of gases. In this model, the porous medium is considered as one component of the mixture and is treated as a collection of giant spherical molecules (dust particles) kept in space by external force. The total flux of a gas mixture is represented as the sum of the diffusive flux (molecular and Knudsen diffusion) and the viscous flux. The DGM in terms of total molar flux can be written as (Thorstenson and Pollock, 1989a):

$$\sum_{j=1, j\neq i}^{n} \frac{y_j N_i^T - y_i N_j^T}{D_{ij}} + \frac{N_i^T}{D_{iK}} = -c_T \frac{dy_i}{dz} - \left(1 + \frac{k_G P}{D_{iK}\mu_G}\right) y_i \frac{dc_T}{dz} \quad (4.56)$$

The first term on the left-hand side of Equation 4.56 considers molecular diffusion, while the second term accounts for Knudsen diffusion. The first and second terms on the right-hand side take into account the driving forces for diffusion (concentration gradient) and advection (total pressure gradient). If the Kudsen diffusion is negligible and there is no total pressure gradient, the DGM is reduced to Stefan-Maxwell equations.

Mean Transport Pore Model (MTPM)

As the DGM, the Mean Transport Pore Model is based on the Stefan-Maxwell equation modified to include Knudsen diffusion and the Darcy's law. The MTPM visualizes pores as cylindrical capillaries with radii distributed around a mean value r. Both models, DGM and MTPM, represent the mass transport due to concentration gradients (pure diffusion) with the same set of differential equations, that is to say:

$$\sum_{j=1, j\neq i}^{n} \frac{y_j N_i^D - y_i N_j^D}{D_{ij}} + \frac{N_i^D}{D_{iK}} = -c_T \frac{dy_i}{dz} \quad (4.57)$$

The model adopted

The diffusive model used in this work is based on Equation 4.57 that we apply to a binary gas mixture:

$$\frac{y_2 N_1^D - y_1 N_2^D}{D_{12}} + \frac{N_1^D}{D_{1K}} = -c_T \frac{dy_1}{dz} \quad (4.58)$$

where the subscript 1 is for CH_4 or H_2O and the subscript 2 refers to CO_2. Using $y_2 = 1 - y_1$ and the Graham's law of diffusion ($-\frac{N_1^D}{N_2^D} = \left(\frac{m_2}{m_1}\right)^{1/2}$; Graham (1833)), Equation 4.58 can be rewritten as:

$$N_1^D = -Dc_T \frac{dy_1}{dz} \qquad (4.59)$$

where

$$\frac{1}{D} = \frac{1}{D_{1K}} + \frac{1 - y_1(1 - \sqrt{\frac{m_1}{m_2}})}{D_{12}} \qquad (4.60)$$

Rewritting Equation 4.59 in terms of mass flux J gives:

$$J_1^D = -D \frac{d\rho_1}{dz} \qquad (4.61)$$

Finally, the mass conservation equation is given by:

$$\frac{\partial \sigma}{\partial t} = \frac{\partial}{\partial z} \left(\frac{\Phi}{\tau} D \frac{\partial \rho_1}{\partial z} \right) \qquad (4.62)$$

where σ is determined as described in section 4.4.1 and the obstruction factor has been added to take into account the change in the diffusion coefficient due to the porous medium.

Application to water vapor transport

The determination of the molecular diffusion coefficient $D_{H_2O-CO_2}$ is made using Equation 4.49, while the Knudsen diffusion coefficient D_{H_2OK} is calculated with Equation 4.47. The variation of the pore radius r with water ice content is computed with the following expression (Mellon and Jakosky, 1993):

$$r = r_0 \sqrt{1 - \frac{\rho_i}{\rho_{ice}}} \qquad (4.63)$$

where r_0 is the mean pore radius ($\sim 10\mu$m) and $\rho_{ice} = 926$ kg m^{-3}.

Adsorption in thermodynamic equilibrium is determined using adsorption isotherms for palagonite (Zent and Quinn, 1997):

$$\rho_a = \rho_b A_s m_{ML} \left(\frac{K_0 P}{e^{-\epsilon/T} + K_0 P} \right)^\nu \qquad (4.64)$$

where ρ_b is the bulk density of the regolith, the specific surface area A_s for palagonite is 17000 m^2 kg^{-1}, the mass per unit surface area of a single adsorbed monolayer of water $m_{ML} = 3 \times 10^{-7}$ kg m^{-2}, $K_0 = 7.54 \times 10^{-9}$,

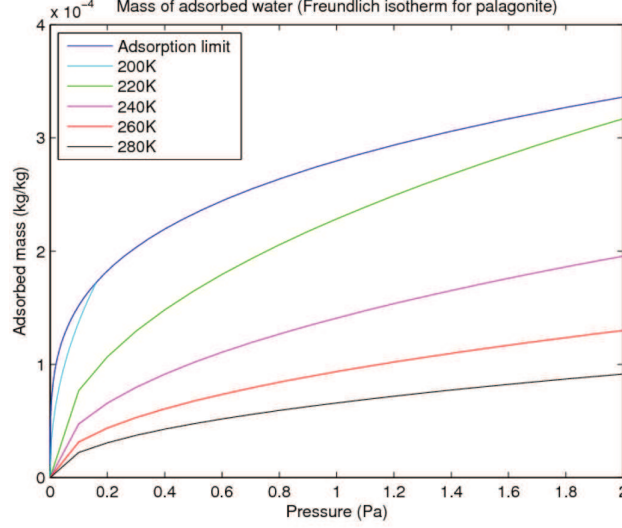$\epsilon = 2697.2$ and $\nu = 0.4734$. These adsorption isotherms are represented in Fig. 4.11.

Figure 4.11: Mass of adsorbed water as a function of H_2O partial pressure.

Combining Equations 4.38, 4.62 and the ideal gas law, leads to:

$$\Phi \frac{\partial}{\partial t} \left(\left(1 - \frac{\rho_i}{\rho_{ice}} \right) \frac{P}{T} + \frac{R}{M} \rho_i \right) + \frac{R}{M} \left(\frac{\partial \rho_a}{\partial P} \frac{\partial P}{\partial t} + \frac{\partial \rho_a}{\partial T} \frac{\partial T}{\partial t} \right)$$
$$= \frac{\partial}{\partial z} \left(\frac{\Phi}{\tau} \left(1 - \frac{\rho_i}{\rho_{ice}} \right)^2 D \frac{\partial}{\partial z} \frac{P}{T} \right) \tag{4.65}$$

where M is the molar mass of H_2O and the term $(1 - \frac{\rho_i}{\rho_{ice}})^2$ takes into account the changes in porosity and tortuosity with ice content (Hudson, 2008). If no ice is present in the subsurface, ρ_i is set to zero and Equation 4.65 determines the partial pressure of water. If ice is present, then the equation is solved for ρ_i using the saturation vapor pressure P_{sat} value for P:

$$P_{\text{sat}} = 611.0 \exp \left(22.5 \left(1 - \frac{273.16}{T} \right) \right) \tag{4.66}$$

The upper boundary condition at the martian surface is given by the partial pressure of water and $\rho_i = 0$, while for the lower boundary condition, we assume zero vapor flux (Schorghofer and Aharonson, 2005). Therefore, H_2O is not allowed to diffuse further down in the soil than our spatial range allows.

Application to methane transport

Combining Equations 4.39 and 4.62, we obtain:

$$\frac{\partial \Phi \rho_G}{\partial t} + \frac{\partial \rho_a}{\partial t} = \frac{\partial}{\partial z} \left(\frac{\Phi}{\tau} D \frac{\partial \rho_G}{\partial z} \right) \tag{4.67}$$

As for water vapor, the Knudsen diffusion coefficient D_{CH_4K} is determined with Equation 4.47 and the molecular diffusion coefficient is calculated similarly to Meslin et al. (2011):

$$D_{CH_4-CO_2} = \frac{3}{8} \sqrt{\frac{\pi}{2\mu_{12}}} \frac{(k_B T)^{3/2}}{P} \frac{1}{\pi \sigma_{12}^2 \Omega(T)} \tag{4.68}$$

where μ_{12} is the reduced mass of the CH_4-CO_2 mixture, σ_{12} is the collision diameter (3.745 $\times 10^{-10}$ m; Boushehri et al. (1987)) and Ω is the diffusion collision integral given by:

$$\Omega(T^*) = \exp(0.295402 - 0510069(\ln T^*) + 0.189395(\ln T^*)^2 \\ - 0.045427(\ln T^*)^3 + 0.0037928(\ln T^*)^4) \tag{4.69}$$

where $T^* = \frac{T}{198.5K}$ (Boushehri et al., 1987).

At equilibrium, ρ_G and ρ_a are linked by the equilibrium rate constant k_{eq} as (Meslin et al., 2011):

$$\left(\frac{\rho_a}{\rho_G} \right)_{eq} = k_{eq}(T) = \frac{\rho_b A_s \bar{v}}{4} \frac{h}{k_B T} \exp \left(\frac{\mid \Delta H \mid}{RT} \right) \tag{4.70}$$

where $\bar{v}$ is the mean thermal speed of CH_4 molecules at temperature T, h is the Planck constant and ΔH = -18.08 kJ mol^{-1} (Gough et al., 2010). Equation 4.67 can therefore be rewritten as:

$$\frac{\partial (\Phi + k_{eq}) \rho_G}{\partial t} = \frac{\partial}{\partial z} \left(\frac{\Phi}{\tau} D \frac{\partial \rho_G}{\partial z} \right) \tag{4.71}$$

The lower boundary condition is defined as a given mass of CH_4 injected at time $t = 0$ or a constant mass flux. At the surface, we assume a zero constant value for methane concentration, which implies that atmosphere is well mixed and remove away methane faster than the diffusion timescale (Stevens et al., 2015).